RESEARCH PAPER

Nature of nonmetallic inclusions in electrogas weld metal

Kangmyung Seo[1,2] · Hoisoo Ryoo[3] · Hee Jin Kim[4] · Joong Geun Yoon[4] · Changhee Lee[2]

Abstract

An electrogas weld metal deposited with an approximately 20 kJ/mm heat input was examined to investigate the chemical and microstructural characteristics of nonmetallic inclusions related to the weld microstructure. The inclusions in this weld were found to be very active for ferrite nucleation, and the larger inclusions tended to be more effective for multiple-nucleation. Experimental evidence demonstrated that the high nucleation potency of inclusions was attributable to the TiO layer formed on the inclusion surface and that the multiple-nucleation was due to the polycrystalline nature of the TiO layer. In addition, small patches of the TiN phase were present on the outer surface of inclusions. From the morphological and chemical composition, this phase was believed to be formed from the steel matrix by the precipitation reaction upon cooling.

Keywords EG weld · Ferrite nucleation · Nonmetallic inclusion · TiO · TiN

1 Introduction

Electrogas (EG) welding is an automatic vertical-up welding process that has been widely employed in shipbuilding industries to improve the welding productivity. This process completes full-thickness welding by a single pass using either one or two electrodes, and thus its heat input increases with the plate thickness, reaching approximately 60 kJ/mm for 80-mm thick plates, more than ten times higher than those of conventional welding processes such as SMAW or FCAW [1–4]. To tolerate such a high heat input in HAZs, steel manufacturers have developed various types of steels ensuring an excellent HAZ toughness in the thick welded

✉ Hee Jin Kim
kimheejin0827@gmail.com

1   Department of Advanced Materials & Chemical Engineering, Hanyang University, 222 Wangsimni-ro, Seongdong-gu, Seoul 04763, Republic of Korea

2   Department of Joining Technology, Korea Institute of Materials Science, 797 Chanwon-daero, Seongsan-gu, Changson-si, Gyeongnam 51508, Republic of Korea

3   Korea Institute of Industrial Technology (KITECH), 156 Gaetbeol-ro, Yeonsu-gu, Incheon 21999, Republic of Korea

4   R&D Center, KISWEL, 704 Gongdan-ro, Seongsan-gu, Changwon-si, Gyeongnam 51544, Republic of Korea

joints produced by tandem (two electrodes) EGW process. These steels include high-nitrogen type TiN steel [5], microalloying TiN steel [6], and oxide-dispersed steel [7].

EG weld metals have also been reported to possess high impact toughness properties associated with the development of fine intragranular structures containing a high volume fraction of acicular ferrite [8–10]. Referring to these results, the inclusions formed in the welds studied were suspected to be very active for nucleating the intragranular ferrite grains, which looked somewhat different from acicular ferrite in morphology. Considering that not all but specific types of inclusions were active for acicular ferrite nucleation [11, 12], the inclusions formed in those EG welds were of interest in terms of their constituent phases relating to ferrite nucleation; however, the inclusion characteristics promoting ferrite nucleation have not been studied in previous investigations [8, 9, 13, 14]. Therefore, this study was conducted to understand the characteristics of nonmetallic inclusions formed in EG weld metals, the microstructure of which was predominant with intragranular ferrite. Specifically, we aimed to determine what type of titanium-containing phases form on the inclusion surface and to clarify if manganese-depleted zone (MDZ) forms or not. In addition, the possible formation of TiN was also examined. The reasons for pursuing these subjects are as follows:

One of the popular approaches widely accepted for the development of consumables with improved toughness would be the addition of titanium as a microalloying element

based on numerous experimental results showing that it promotes the formation of acicular ferrite [15–21]. To understand its effect, many investigators have tried to identify the phases formed at the inclusion/matrix interface in particular because, in titanium-containing welds, titanium-rich phases were often found to be formed on the inclusion surface and thus were reasonably suspected to be responsible for ferrite nucleation. Based on these studies, several phases, such as TiO [15, 17, 22], TiN[17, 23], TiC [24], or $MnTi_2O_4$ [25], have been recognized with some quantitative results.

Finally, Yamada et al. [26] identified a titanium-containing layer phase formed on the surface of composite inclusions of spinel oxide ($MnAl_2O_4$) and amorphous manganese silicate to be TiO by selected area diffraction (SAD) analysis via transmission electron microscopy (TEM). It was also found that the Baker-Nutting (B-N) orientation relationship existed between the TiO layer and the adjacent ferrite grains, and this finding could enable the low misfit theory to be the most appropriate mechanism for nucleating ferrite plates at inclusions. After this pioneering work, their results were confirmed repeatedly by subsequent studies [27, 28]. In particular, Fujiyama et al. [28] further claimed that, in addition to the B-N relationship, the TiO coating layer created MDZs around the inclusions, which was not mentioned in earlier studies [26, 27]. Therefore, MDZ formation associated with the TiO layer is currently a controversial issue, in contrast to the full agreement for Ti_2O_3 inclusions [29–31].

Another type of titanium-rich phase often reported to be formed on the surface of titanium-containing inclusions is $MnTi_2O_4$. This phase was first expected to be formed in the inclusions of welds containing a minimal level of titanium based on the results obtained by the semi-quantitative measurement of the chemical composition [25] and later verified as $MnTi_2O_4$ having a B-N orientation relationship with adjacent ferrite by the SAD analysis in TEM [32]. This type of phase was also found in the high-titanium welds but was not in agreement on MDZ formation either [19, 33, 34]. Therefore, in titanium-containing welds, the two current issues with the ferrite nucleation are (1) which type of titanium-containing phase forms on the inclusion surface and (2) whether the MDZ formation takes place or not.

Another issue that has been discussed for a long time in the titanium-containing welds is the formation of TiN phase [23, 35, 36]. When it forms on the inclusion surface, the nucleation potency of inclusions can be enhanced as it has good lattice matching with ferrite. However many researchers failed to find clear evidence for TiN formation even in the high nitrogen welds [17, 37, 38]. This failure was most likely due to the phase being small in size compared to the spatial resolution limit of the analytical microscopes employed [25].

One of the consequences resulting from the high heat input welding is the extension of the weld pool retention time which in turn provides the inclusion particles with a longer time to grow before solidification. Indeed, it has been shown experimentally that the inclusion size was directly proportional to the cube root of the heat input as predicted by theoretical calculations [23]. Accordingly, it was thought in the present study that the large-size inclusions most likely to be formed in EG welds would facilitate more convincing analysis of inclusion substructures, especially the phase formed on the inclusion surfaces if any. With the slow cooling rate in EG welds, both MDZ and TiN precipitates were also anticipated to be grown thicker with a longer time available for diffusional reactions.

Consequently, EG welds made with high heat input have at least two advantages with respect to the inclusion analysis: the increased size of inclusions due to the longer retention time and the promotion of diffusion-controlled products by the slower cooling rates. By virtue of these, this study aims to investigate the current issues of inclusions for ferrite nucleation: (1) the type of titanium-containing phase contributing to ferrite nucleation, (2) the presence or absence of MDZ formation around the inclusion, and (3) the possible formation of TiN phase on the inclusion surface.

2 Experimental procedure

Of the EG welds investigated in the previous study [8], one designated "one-pole EG(25t)" was selected for this study because it showed a weld microstructure wholly comprised of intragranular ferrite and with little formation of coarse constituents such as grain boundary ferrite and ferrite with a second phase. As noticed in its designation, this weld was fabricated by the one-pole EG process with 25-mm thick A516-70 base plates using 20 kJ/mm heat input.

Figure 1 illustrates the one-pole EG welding process. In this process, flux-cored wire of normally 1.6 mm in diameter is fed into a cavity formed by the groove faces of the plates to be welded. The groove openings are covered with the water-cooled copper shoe on the front surface side of the groove and a ceramic backing material attached on the backside of the plates. As the cavity fills, the retaining copper shoe moves upward with the welding gun. For the present EG weld made for 20-mm thick plates with 20 kJ/mm heat input, the cooling rate from 800 to 500 °C was estimated to be 220 s using the master curves given in Reference [39]. This cooling time is extremely long compared to those of SMAW and GMAW, in which it is approximately several tens of seconds.

The macro- and microstructures of the present weld are shown in Figs. 2(a) and (b), respectively. The weld microstructure consists of a mixture of acicular ferrite and polygonal ferrite, both of which are called "intragranular ferrite." Such a fine microstructure with the absence of coarse constituents such as grain boundary ferrite and
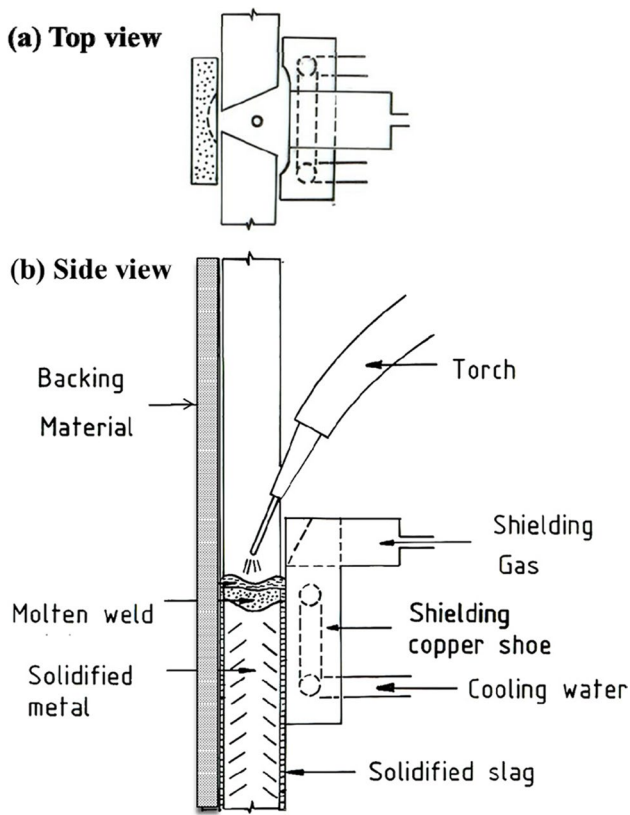
Fig. 1 Schematic illustration of one-pole EG welding process

ferrite side plates resulted in a high toughness weld metal. The Charpy impact energy reported at weld center was 120 J at − 20 °C, and the ductile–brittle transition temperature was approximately − 60 °C [8]. The chemical composition quoted from the previous report is given in Table 1, along with that of the SMAW specimen selected from the specimens previously investigated by the present authors [32]. This weld was made with 1 kJ/mm heat input and therefore assumed to be good for a reference of a low heat input weld. As noticed in Table 1, these two welds have very similar oxygen contents.

Size measurements of ferrite grains and inclusions were performed by field-emission scanning electron microscopy (FE-SEM, model JEOL JSM-7100F) using a metallographic specimen taken from the weld center. The average grain size was determined by electron backscatter diffraction (EBSD) analysis in SEM by means of the area mode. The nucleation probability of inclusions was also determined using the same experimental procedure as described in Reference [40]. The chemical heterogeneity of the inclusions was analyzed by energy dispersive X-ray spectroscopy (EDS) equipped with SEM. For the details of inclusion constituent phases, thin foil samples were prepared by the focused ion beam (FIB) method and examined using an analytical transmission electron microscope (ATEM, model JEOL JEM-2100F) at an operating voltage of 200 kV. Of particular interest were the internal structures of the inclusions and the nature of the inclusion/matrix interface. In addition to the selected area diffraction (SAD) examination, chemical analyses were performed employing EDS for the major elements and electron energy loss spectroscopy (EELS) for the light elements such as oxygen and nitrogen.

Fig. 2 EG weld investigated in this study: (**a**) three-dimensional view of specimen with the macrostructure revealed on the cross section and (**b**) optical microstructure taken at the central region of weld metal etched with 2% Nital solution
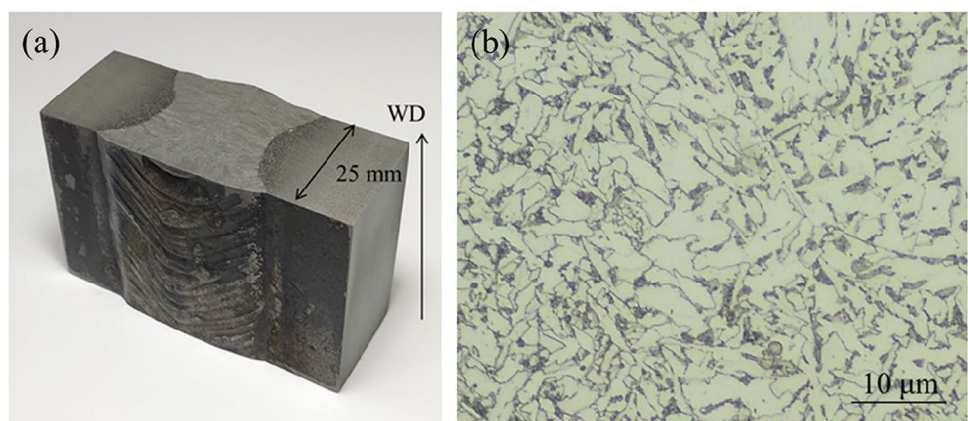

Table 1 Chemical composition of welds used in this study

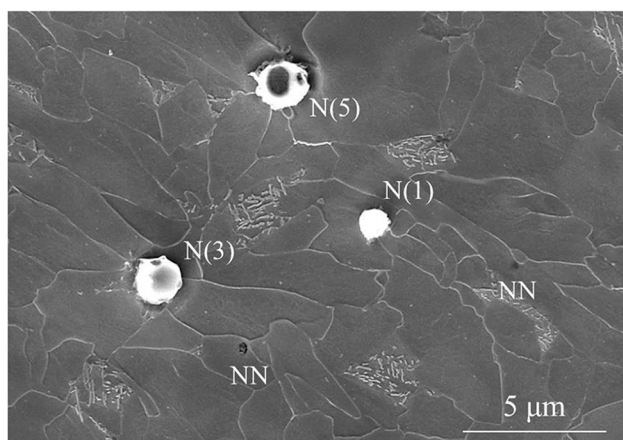| ID	C	Si	Mn	Ni	Ti	Al	B	O	N
EGW	0.09	0.16	1.33	1.17	0.035	0.011	0.0039	0.0394	0.0022
SMAW	0.09	0.38	1.63	-	0.003	-	0.0002	0.0430	0.0079

Fig. 3 SEM microstructure showing ferrite grain structure and inclusions of nucleant (N) and non-nucleant (NN)

3 Results and discussion

3.1 SEM microstructure

After the optical observation given in Fig. 2(b), the same specimen was electroetched in a solution of acetic acid mixed with 20% perchloric acid for the SEM observation. Figure 3 shows a typical SEM microstructure taken at a high magnification, depicting a matrix structure composed of ferrite and pearlite and several inclusions quite different in size. Due to the elongated and irregular shape of ferrite grains, their sizes were measured by EBSD in the area mode. The average of three measurements determined with a 15° tolerance angle turned out to be 4.0 ± 0.24 μm. For inclusions, the average size was determined to be 0.83 μm, which was much greater than that of SMAW (0.32 μm). These two results were well matched with the theoretical predictions proposed by Kluken and Grong [23]. It is worth mentioning that as expected, large inclusions over 3 μm in size were not that difficult to find in the present EG weld.

3.2 Ferrite nucleation

Another thing to note in Fig. 3 is that three out of five inclusions acted as the nucleation sites for ferrite, while the other two small inclusions (marked as NN) did not. This fact indicates that the inclusion size affects the nucleation potency of inclusions and increases with the inclusion size. Following thermodynamic prediction [41], such a positive effect of inclusion size on nucleation potency has been well demonstrated by many researchers [40, 42]. To confirm this effect, a total of 750 inclusions observed in SEM were classified into nucleant (N) or non-nucleant (NN) and measured for their size. Then, the nucleation probabilities at a given size-interval were plotted as a function of inclusion size as

reported elsewhere [40, 42]. As expected, the result depicted in Fig. 4 shows that the nucleation probability increases with the inclusion size and reaches 100% when the inclusions are over a critical size of 1.1 μm, which is quite higher than that of SMAW weld. In the case of small inclusions, therefore, SMAW probabilities are higher than EGW ones. However, as the proportion of small inclusions were far lower in the EG weld than in the SMAW weld, the total nucleation probability of the EG weld was 69% which was higher than that of the SMAW weld (55%). These are the results obtained from the two-dimensional observation, and thus the actual probability would be increased to a greater extent when measured in three-dimensional views.

Figure 3 also shows a significant difference in the number of ferrite grains nucleating from each inclusion. In this two-dimensional observation, several ferrite grains are apparent to be formed from the large inclusions such as N(5) and N(3), but no ferrite can be seen from small inclusions marked by NN. Another SEM image of multiple-nucleation is presented in Fig. 6(a), where six ferrite grains appear to fan outward from the inclusion of 3.4 μm in size. Such a feature of multiple-nucleation was often reported in the literature [36, 40, 43]; however, little attention seemed to be paid to "how multiple-nucleation takes place." In Reference 40, for example, the effect of inclusion size on the ferrite numbers was acknowledged, but no plausible explanation was made.

To confirm the possible effect of inclusion size, another data set was constructed from approximately 200 inclusions, and then the number of ferrite grains counted for each inclusion was plotted as a function of inclusion size. The results are presented graphically in Fig. 5. Although the scatter in individual measurements is large, the general trend of ferrite numbers is seen to increase with increasing inclusion size until reaching the maximum number of eight.
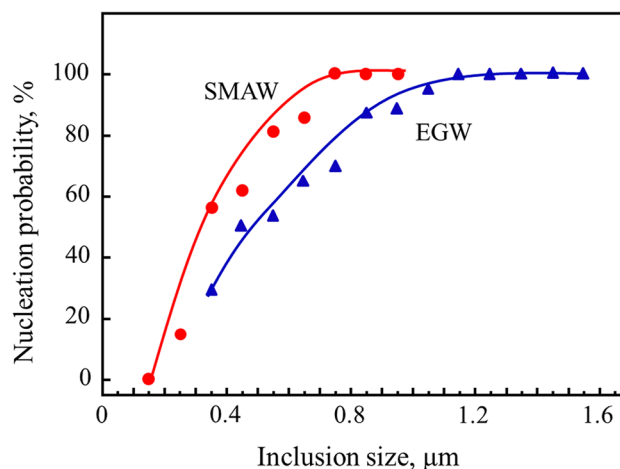

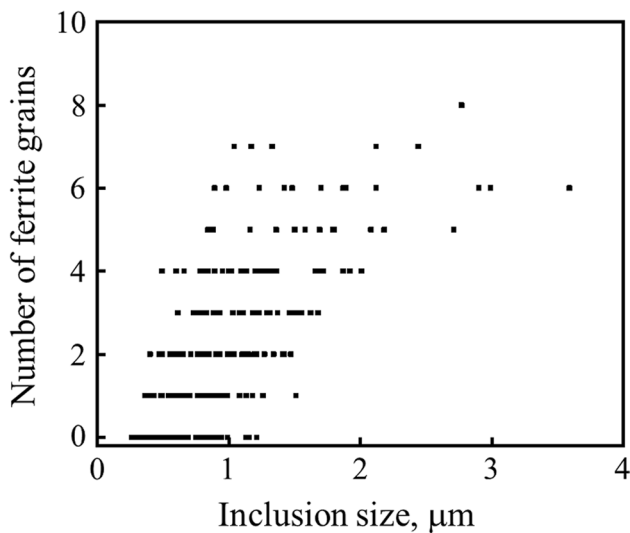**Fig. 4** Nucleation probabilities plotted as a function of inclusion size

Fig. 5 Effect of inclusion size on the number of ferrite grains nucleated

3.3 Inclusions analysis by SEM

In SEM, a cursory look at a low magnification revealed that inclusions were spherical in shape as shown in Fig. 6(a), but at high magnification, their surfaces were finely faceted, as shown in Fig. 6(b). Faceted growth was suspected to occur as a result of anisotropy in the growth rates between high-index and low-index crystallographic planes [44]. This implies that the present inclusions have crystalline phases exposed on the surface. To identify the constituent phases formed in inclusions, SEM/EDS analyses were performed on the cross-sections of rather large inclusions, the sizes of which were over 3 µm. The SEM image in Fig. 7 represents a typical structure of inclusion in which several granular particles are engulfed by the matrix phase. The EDS elemental mapping results demonstrate that the matrix phase is an oxide rich in aluminum and silicon, while the granular particles

embedded in the matrix are nearly pure titanium oxide. In addition, islands of MnS are present in the peripheral region of inclusion and an aluminum-rich oxide particle within the matrix phase. Most importantly, as evident in the titanium image, all the inclusions examined were almost entirely covered with the titanium-rich phase regardless of their size. To the best of the present authors' knowledge, such an image of the titanium layer has not been achieved at the resolution level of SEM/EDS but, to date, has been obtained only at the high resolution of TEM/EDS [26, 27, 30, 31]. Thus, the present achievement is believed to be obtained by virtue of the increased thickness of titanium-rich layer with the high heat inputs of EG welding.

3.4 Inclusion analysis by ATEM

To identify the nature of the titanium-rich layer and other phases, two TEM specimens were extracted by the FIB system from the inclusions including the one examined in Fig. 7, where the location of the TEM specimen is marked with a dotted line in the SEM image. The TEM and STEM images in Figs. 8(a) and (b) show the overall features of the inclusions that include the faceted inclusion surface and heterogeneity of the inclusion phases. From EDS mapping images in Figs. 8(c)–(f), it is clear that this inclusion consists of at least five phases: a matrix phase of manganese-rich oxide, two oxide particles rich in either titanium or aluminum, islands of MnS near the inclusion surface, and a titanium-rich layer formed along the inclusion surface. The chemical compositions of these phases determined by EDS and the crystal structure by SAD analysis are given in Table 2. The matrix phase was confirmed to be an amorphous oxide containing manganese, aluminum, and silicon, which is indicative of aluminum-containing manganese silicate, i.e., (Mn,Al)-silicate. The aluminum-rich oxide particle formed in an angular shape was Al_2O_3 containing a small amount of manganese and magnesium. The titanium-rich oxide particles with a granular shape were Ti_2O_3 containing

Fig. 6 SEM micrographs taken from a typical inclusion acting for multiple-nucleation at (**a**) low and (**b**) high magnifications
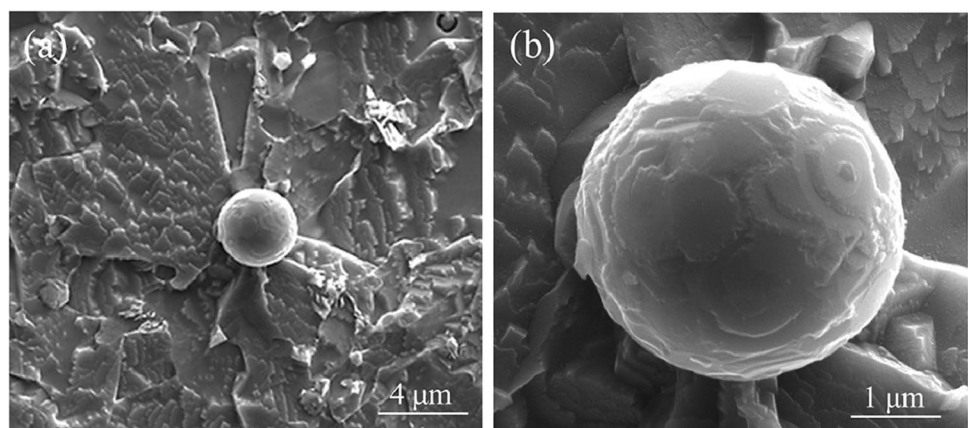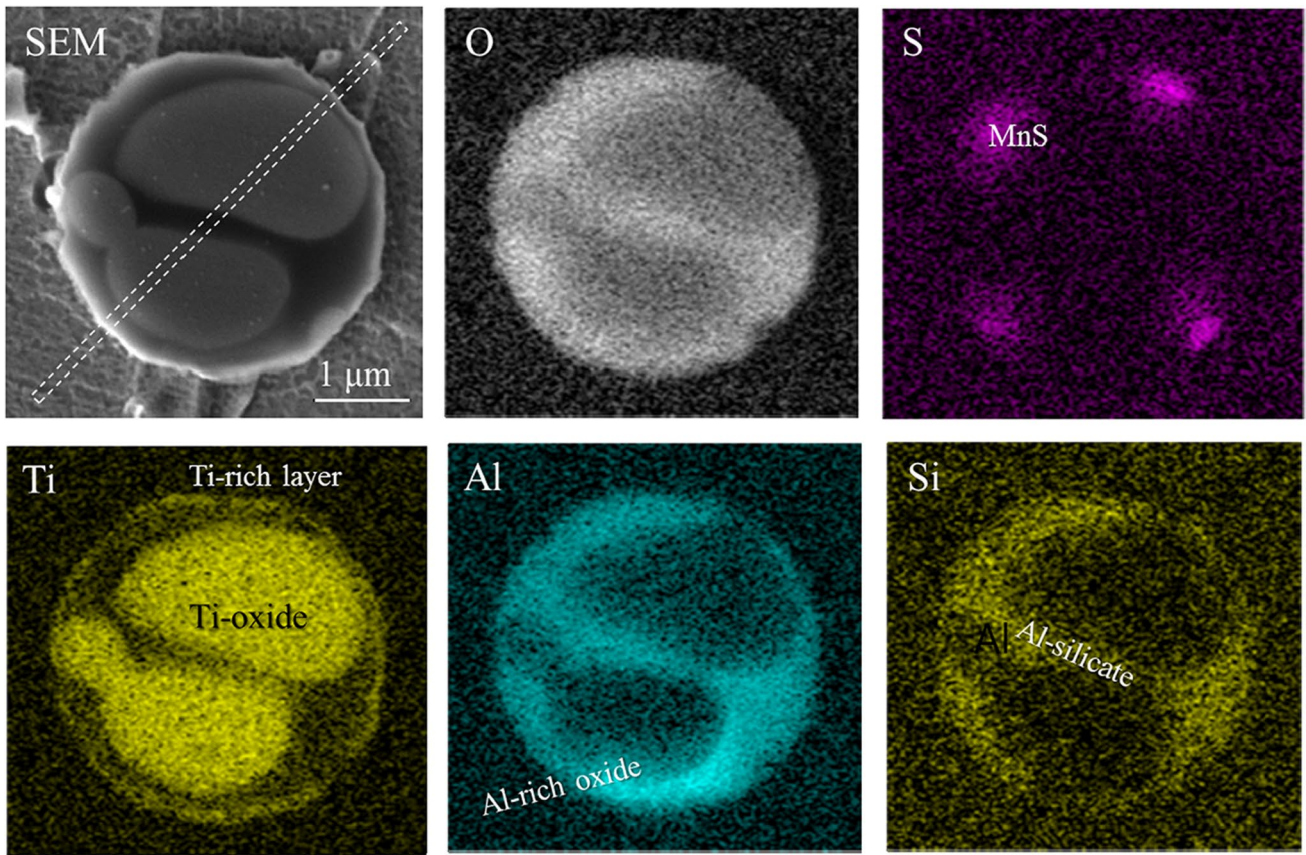
Fig. 7 SEM and EDS results obtained on the cross-section of the inclusion acting as nucleation site of multiple ferrites. Dotted line in SEM image indicates the location of TEM specimen being extracted
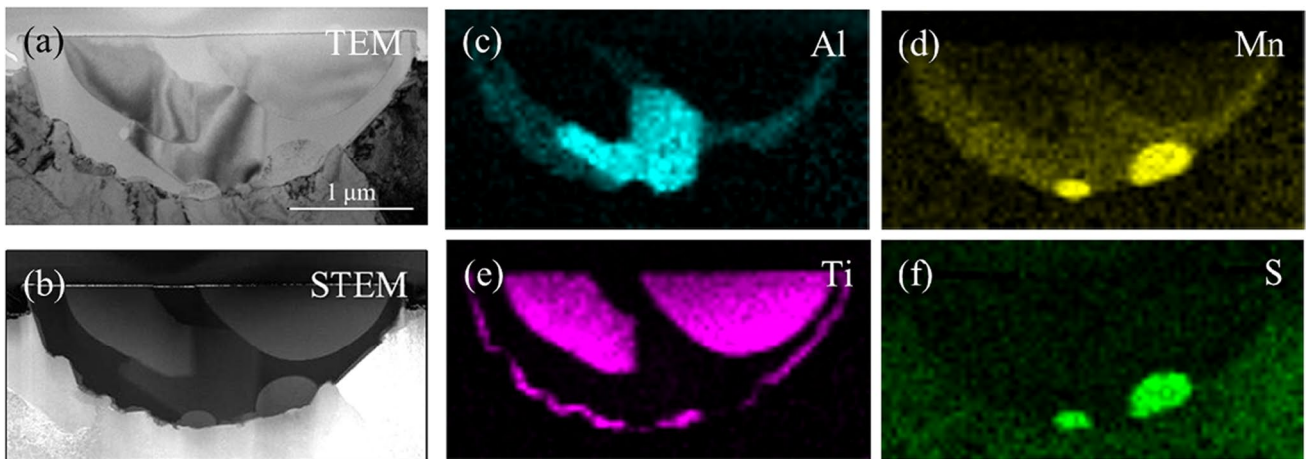

Fig. 8 ATEM results of the inclusion shown in Fig. 7: (**a**) TEM image, (**b**) STEM image, and EDS elemental mapping images of (**c**) aluminum, (**d**) manganese, (**e**) titanium, and (**f**) sulfur

some manganese. No nitrogen was detected in these particles. In the case of the titanium-rich layer, an additional examination was performed at a high magnification to identify its phase characteristics.

Figure 9(a) shows a high-magnification STEM image taken from the left part of the inclusion shown in Fig. 8. From this image, it is manifested at a glance that the titanium-rich layer is not uniform in thickness at all; some part

Table 2 Chemical composition determined by EDS in wt.% and phases identified by SAD analysis in TEM

Phase	EDS analysis, wt %							SAD analysis
	Al	Ti	Mn	Si	Mg	O	N	
(Mn,Al)-silicate	10.2	1.0	18.5	6.1	1.3	59.9	Detected	Amorphous
Al-oxide	29.9	1.6	12.4	0.4	6.5	46.9	Detected	Al_2O_3
Ti-oxide	1.0	48.4	6.8	1.4	0.3	38.9	Not detected	Ti_2O_3
Ti–rich layer	2.6	54.8	3.7	3.9	0.0	31.8	Detected	TiO

Fig. 9 TEM and EDS results of titanium-rich layer: (**a**) STEM image showing the morphology of titanium-rich layer and (**b**) and (**c**) results of EDS line scanning across the layer following the red line in (**a**)
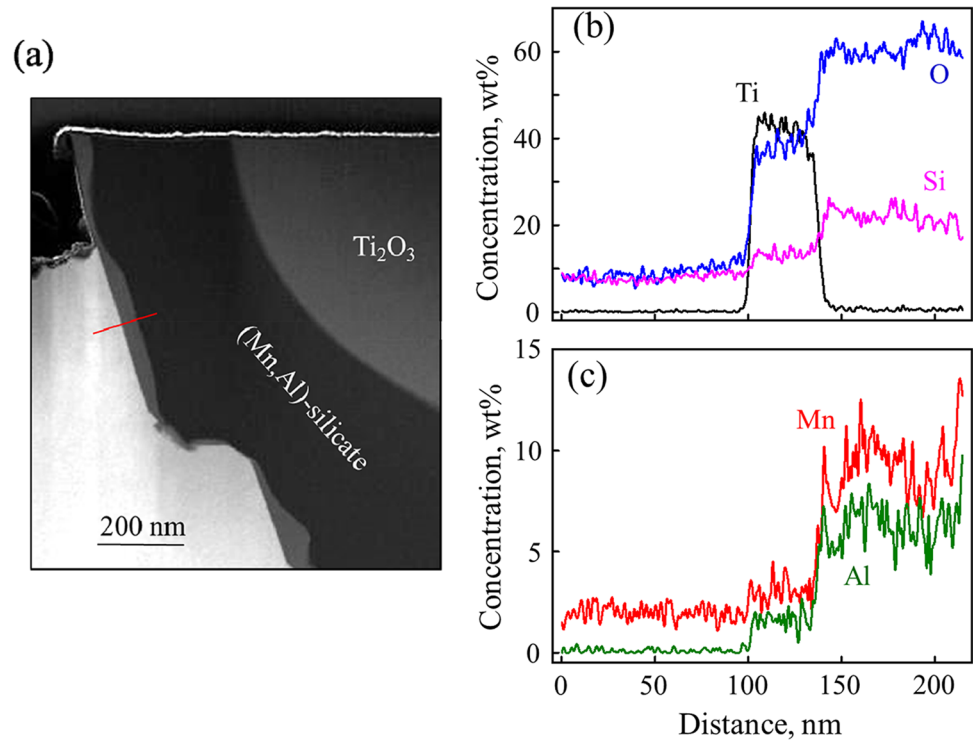
of this layer is as thick as 80 nm. In contrast to the outer surface, the inner surfaces are curved with bulges growing toward the silicate matrix and forming a thicker part of the layer. This region facilitates the reliable analysis of its chemistry, as shown in Table 2.

The chemical nature of the titanium-rich layer was further studied by EDS line scanning across the layer starting from the left side, as marked by the red line in Fig. 9(a), and the results are exhibited in Figs. 9(b) and (c). These results demonstrate that the layer is very high in oxygen and contains a small amount of other elements. Thus this layer was confirmed to be titanium oxide alloyed with silicon, manganese, and aluminum. In the EDS spectrum, a small nitrogen peak was also observed, indicating that the titanium oxide layer contains some nitrogen. Further details on the nitrogen alloying will be described in the EELS results later.

As there are various forms of titanium oxide such as TiO, TiO_2, and Ti_2O_3, extensive SAD analysis was performed to identify its phase. Based on the results of SAD and dark-field analysis shown in Figs. 10(b) and (c), the

titanium oxide layer is firmly identified to be the TiO phase, which possesses B-N orientation relationship with the adjacent ferrite, as reported by others [26, 28]. The high-resolution lattice image in Fig. 11 also demonstrates the possession of B-N relationship by displaying the parallel feature between the (200) planes of TiO and ferrite. Another example of an inclusion showing the nature of the TiO layer is displayed in Fig. 12. As shown in the darkfield image, this TiO layer is a single crystal (or grain) and sufficiently long enough to cover several facets; however, this TiO layer generates just one ferrite grain having B-N relationship with TiO grain.

From the morphological features of the TiO layer and its EDS results described above, it can be inferred that the TiO layer is formed by crystallization from the liquid (Mn,Al)-silicate phase, possibly due to the decreased solubility of titanium in liquid silicate phase upon cooling. If this is the case, the steel interface would provide TiO with heterogeneous nucleation sites, as the melting temperatures of silicate phases are known to be lower than the steel matrix [45].
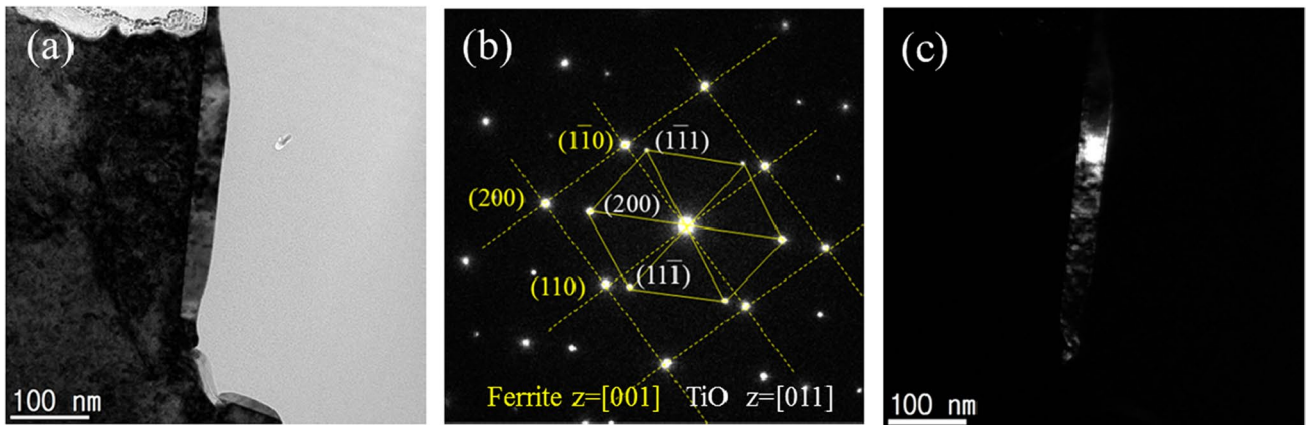
Fig. 10 Result of SAD analysis of the titanium oxide layer: (**a**) bright field image, (**b**) SAD pattern, and (**c**) dark-field image taken from (200) spot
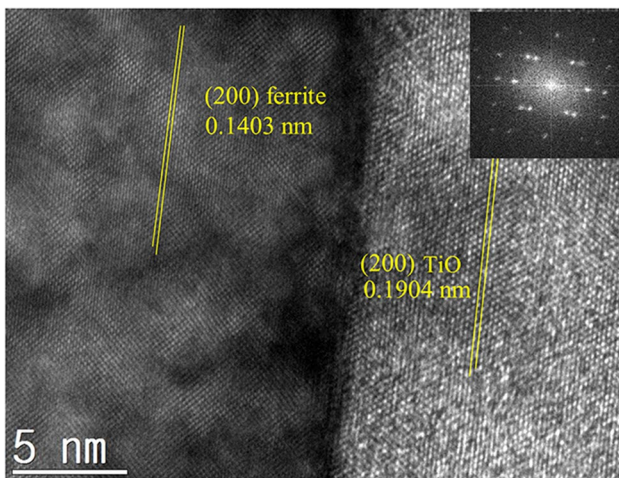

Fig. 11 High-resolution lattice image taken at the ferrite/TiO interface in Fig. 10

One thing to note in Fig. 9(c) is the concentration profile of manganese that exhibits little variation in the steel matrix, implying that no MDZ formation takes place in the present inclusions. As mentioned earlier, however, Fujiyama et al. [24] reported in SAW weld metals that MDZ formed in front of the inclusion surface covered with TiO layer. They explained the reason for its formation being the same as that of Ti_2O_3; on cooling, the TiO phase can absorb manganese from the steel matrix, which is called the "cation vacancy effect" for Ti_2O_3 [46]. Considering the distinct discrepancy between the two results, we examined one more inclusion but failed to find any indication of MDZ formation. The reason for this discrepancy is not fully understood; however, it may have something to do with the welding processes employed and partly the manganese content of the welds. Even if the MDZ develops by the cation vacancy effect after solidification, the far slower cooling rate in EGW than in

Fig. 12 TEM micrographs showing the TiO layer extending over the several facets: (**a**) BF image of ferrite grain and inclusion and (**b**) dark-field image of TiO layer taken from the box area in (a)
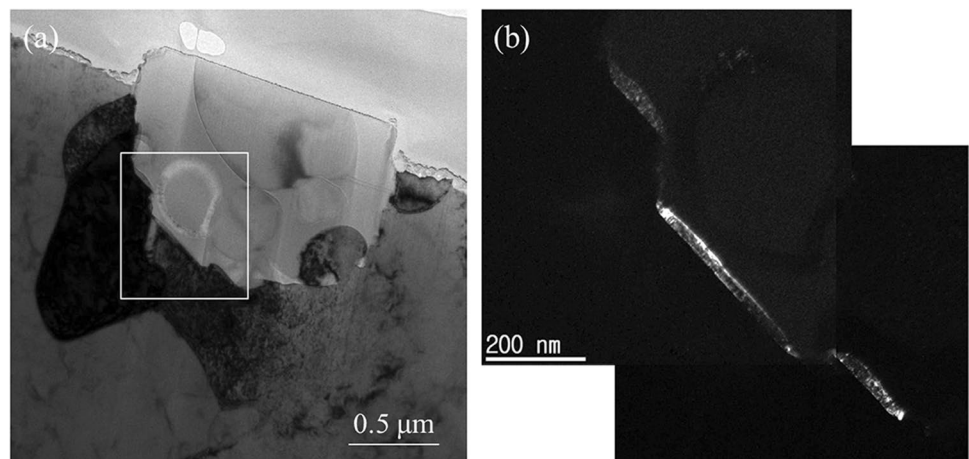
SAW will promote manganese diffusion into the depleted regions to a greater extent and thus obviate or heal up the MDZ eventually.

3.5 Multiple-nucleation of acicular ferrite

Figure 13(a) shows the bright field image of the ferrite plate examined in Fig. 10. This image was taken at a low magnification to illustrate the whole view of the ferrite plate (designated ferrite 1) at a zone axis of z = [001]. This ferrite was the one grown from the left side of the inclusion. Two more ferrites marked ferrite 2 and 3 were observed in the other part of the inclusion surface, and their bright field images taken at each of their zone axis z = [001] are shown in Figs. 13(b) and (c). In their SADs, it is clear that they exhibit the B-N orientation relationship with their underlying TiO layer. Due to the absence of MDZ formation, it can now be concluded that the low misfit theory is the major mechanism operating for ferrite nucleation in this weld.

It is important to note in Fig. 13 that the three SAD patterns of TiO are all different in orientation. This fact implies that the TiO layer present on the inclusion surface
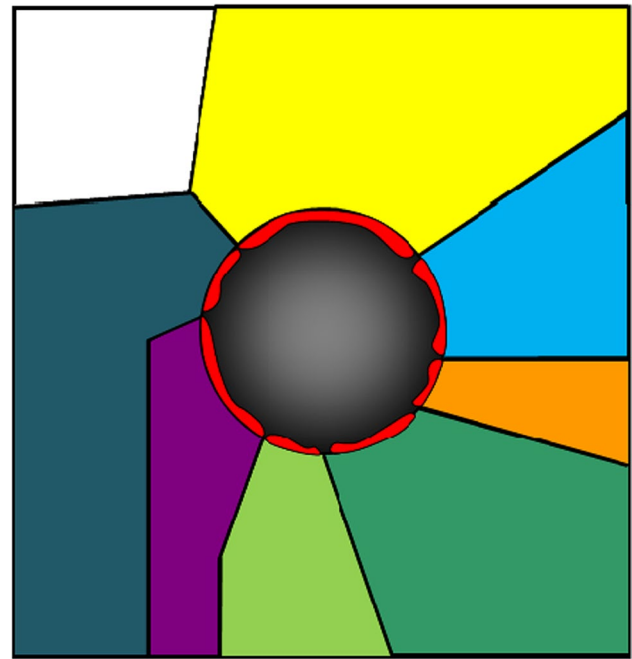

Fig. 14 Schematic illustration of multiple-nucleation attributable to the polycrystalline nature of TiO layer
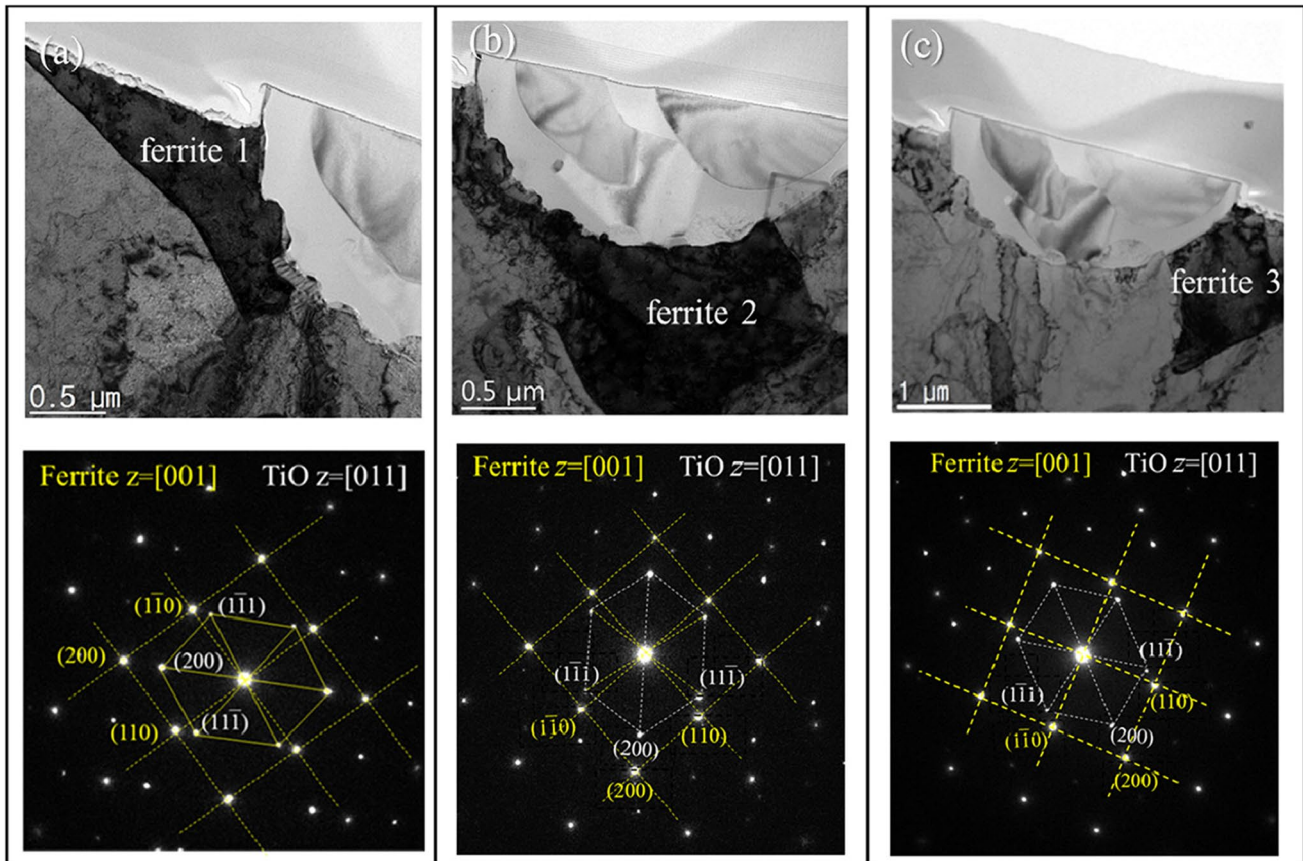

Fig. 13 Result of SAD analysis for each of three ferrites formed on the inclusion surface

is not in the form of a single crystal but composed of three grains; each of these three grains nucleates its own ferrite following the B-N orientation relationship. This result indicates that the number of ferrites may be equal to the number of TiO grains formed on the surface of the inclusions. Such a one-to-one relation between ferrite and TiO grains can explain how the single inclusion shown in Figs. 3 and 6(a) can produce many ferrite plates, all being different in orientation. The one-to-one relation with the polycrystalline TiO layer is schematically illustrated in Fig. 14, where seven TiO layer grains are assumed to be formed on the inner surface of the inclusion, and this number would be controlled by many unknown factors. However, in this study, it was of interest to consider the one-to-one relation in terms of the inclusion size. Considering that the surface area increases with the inclusion size, it is most likely that the larger the inclusion, the more TiO grains nucleate from the inclusion surface; this in turn activates the inclusion to nucleate more ferrite plates, as demonstrated in Fig. 5.
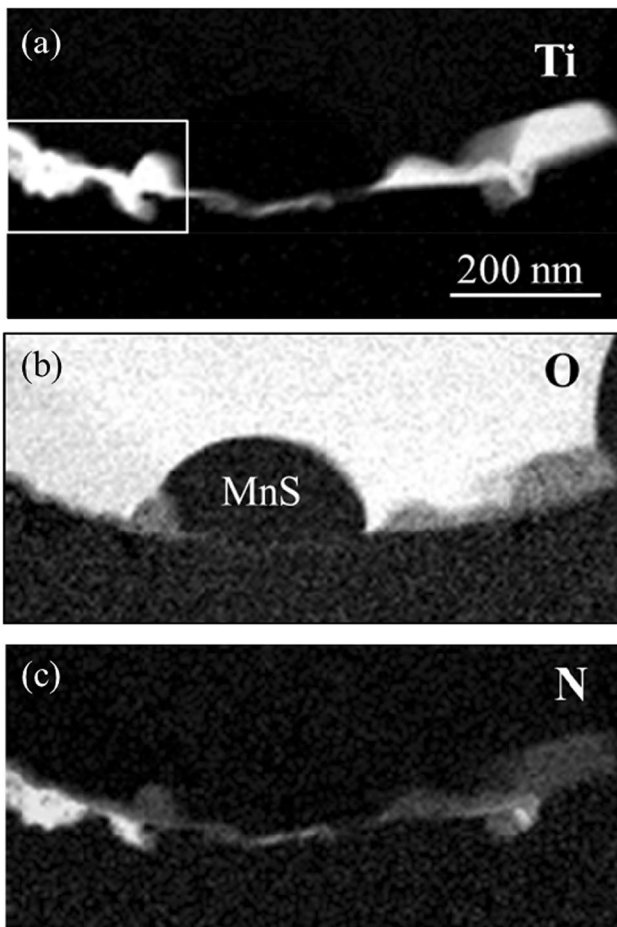
3.6 TiN precipitation

As mentioned earlier, TiN has long been believed to be formed possibly on the inclusions even with little evidence reported in the open literature. Indeed, the characterization of the thin layer is difficult due to the superposition of other phases as well as the limited spatial resolution of EDS in TEM. To cope with these challenges and to understand the

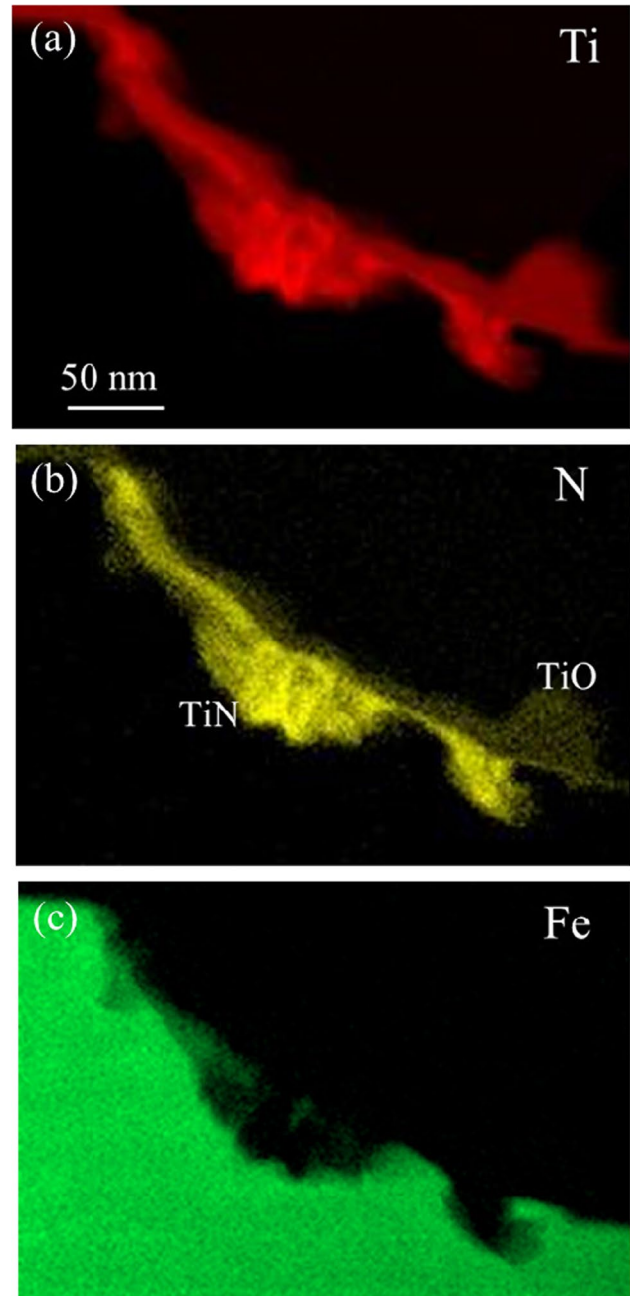**Fig. 16** EELS mapping images taken from the box area in Fig. 15(a): (**a**) titanium, (**b**) nitrogen, and (**c**) iron

Fig. 15 EELS mapping images taken from the lower part of inclusion shown in Fig. 8: (**a**) titanium, (**b**) oxygen, and (**c**) nitrogen

source of nitrogen detected from the TiO layer (Table 2), an EELS examination was performed after thinning the specimen by iron milling, which provides a homogeneous chemical volume through the thickness. The EELS examination has a special advantage for this study in that the absorption edges for oxygen, nitrogen, and titanium in an EELS spectrum are better separated than those in an EDS spectrum, resulting in more precise and reliable analysis for these elements.

The images in Fig. 15 are the results of EELS mapping for titanium, oxygen, and nitrogen. As shown in Figs. 15(a) and (c), several patches of titanium nitride formed on the inclusion surface and bulged outward. As this phase contains very little oxygen, it is believed to be TiN. On the other hand, as mentioned in the EDS/SEM results, the TiO layer formed on the inner side of the surface also contains nitrogen although its content appeared to be very low. Another fact found at high magnification was that the TiN phase was partly intermixed with iron, as shown in Fig. 16. From the morphological and chemical features shown in Figs. 16(a) and (c), it was inferred that this TiN phase precipitated from the steel matrix upon cooling and thus formed on the outer surface of inclusions as discrete patches. The nitrogen mapping image in Fig. 16 also reconfirms that the TiO layer contains nitrogen to some extent. Therefore, the titanium-rich layer observed in the EDS mapping images in Figs. 7 and 8 can be concluded to be not a single phase but composed of two separated layers: a nearly continuous TiO layer formed on the inner side of the surface and discrete TiN patches on the outer side of the inclusion surface.

4 Conclusion

The major conclusions that can be drawn from this investigation are as follows:

(1) Inclusions formed in the present EG weld were mostly covered with the TiO layer, making the inclusion active for ferrite nucleation, as it has the B-N orientation relationship with the adjacent ferrite. This fact supports the low misfit theory as a major mechanism operating in this weld for ferrite nucleation.

(2) Multiple-nucleation takes place from a single inclusion since the TiO layer formed is polycrystalline in nature and each TiO grain can act as nucleation site of its own ferrite having the B-N relationship. As a result, the number of ferrite grains nucleated increases with the inclusion size as the number of TiO grains increases with increasing the surface area.

(3) Even with the duplicate experiments, no evidence of MDZ formation was obtained for the TiO layer even though it contained a small amount of manganese. This result is quite contrary to others. Therefore, the role of TiO on MDZ formation needs further clarification.

(4) Patches of TiN phase formed on the external surface of inclusions by the precipitation reaction from the steel matrix on cooling and thus partly covered the TiO layer, indicating that the amount of TiN phase formed can affect the nucleation potency of inclusions.

Declarations

Conflict of interest The authors declare no competing interests.

References

1. Norcross JE (1965) Electroslag/Electrogas welding in the free world. Weld J 44(3):177–186
2. Takeuchi N, Nagashima M, Tsuruga S (1985) Automated welding in tank construction and its cost-reducing effect. Weld J 84(2):18–29
3. Sasaki K, Suda K, Motomatsu R, Hashiba Y, Ohkita S, Imai S (2004) Development of two-electrode electrogas arc welding process. Nippon Steel Tech Report 90:67–74
4. Ryu K-M, Kim D-W, Lee J-W, Bang H-C, Park C-K, Jeong H (2017) High heat input electrogas welding of TMCP plate for steel storage tanks. J Weld Join 35(6):27–31 (**in Korean**)
5. Jeong HC, An YH, Choo WY (2002) The effect of TiN particles on the HAZ microstructure and toughness in high nitrogen TiN steel. Int J KWS 2(1):25–28
6. Suzuki S, Ichimiya K, Akita T (2005) High strength steel plates with excellent HAZ toughness for shipbuilding - JFE EWEL technology for excellent quality in HAZ of high heat input welded joints. JFE Technical Rep 5:45–52
7. Minagawa M, Ishida K, Funatsu Y, Imai S (2004) 390 MPa yield strength steel plate for large heat-input welding for large container ships. Nippon Steel Tech Rep 90:7–10
8. Seo K, Ryoo H, Kim HJ, Yoon JG, Lee C (2020) Characterization of the local brittle layer formed in electro-gas weld metals. Weld World 65(3):513–524
9. Hashiba Y, Kojima K, Kasuya T, Kumagai T (2015) Development of welding consumables and welding process for newly developed steel plates. Nippon Steel Sumitomo Metal Tech Rep 110:90–96
10. Banaschik R, Herholz H, Henkel K-M (2015) Flux-cored wire electrodes for electrogas welding in the European economic region-Current development status. Schweissen Schneiden 67(5):243–249
11. Sarma DS, Karasev AV, Jönsson PG (2009) On the role of non-metallic inclusions in the nucleation of acicular ferrite in steels. ISIJ Int 49(7):1063–1074
12. Loder D, Michelic SK, Bernhard C (2017) Acicular ferrite formation and its influencing factors-A review. J Mater Sci Res 6(1):24–43
13. Lee J-S, Yun J-O, Jeong S-H, Park CG, An YH (2010) The study about characteristics of welding consumables and weld metal for EGW. J KWJS 28(2):199–203 (**in Korean**)
14. Jeong HC, Park YH, An YH, Lee JB (2007) Mechanical properties and microstructures of high heat input welded tandem EGW joint in EH36-TM steel. J KWJS 25(1):57–62 (**in Korean**)
15. Ito Y, Nakanishi M (1976) Study on Charpy impact properties of weld metal with submerged arc welding. Sumitomo Search 15:42–61

16. Horii Y, Ichkawa K, Ohkita S, Funaki S, Yurioka N (1995) Chemical composition and crystal structure of oxide inclusions promoting acicular ferrite transformation in low alloy submerged arc weld metal. Quarterly J JWS 13(4):500–507

17. St-Laurent S, L'Esperance G (1992) Effects of chemistry, density and size distribution of inclusions on the nucleation of acicular ferrite of C-Mn steel shielded-metal-arc-welding weldments. Mater Sci Eng A149:203–216

18. Jiang QL, Li YJ, Wang J, Zhang L (2011) Effects of Mn and Ti on microstructure and inclusions in weld metal of high strength low alloy steel. Mater Sci Technol 27(9):1385–1390

19. Nako H, Hatano H, Okazaki Y, Yamashita K, Otsu M (2014) Crystal orientation relationship between acicular ferrite, oxide, and the austenite matrix. ISIJ Int 54(7):1690–1696

20. Evans GM (1991) The effect of titanium in SMA C-Mn steel multipass deposits. Weld J 71(12):447s–454s

21. Evans GM (1993) The effect of titanium in manganese-containing SMA weld deposits. Weld J 72(3):123s–133s

22. Mills AR, Thewlis G, Whiteman JA (1987) Nature of inclusions in steel weld metals and their influence on the formation of acicular ferrite. Mater Sci Tech 3:1051–1061

23. Kluken AO, Grong Ø (1989) Mechanisms of inclusion formation in Al-Ti-Si-Mn deoxidized steel weld metals. Met Trans A 20A(8):1335–1349

24. Es-Souni M, Beaven PA (1990) Microanalysis of inclusion/matrix interfaces in weld metals. Surf Interface Anal 16:504–509

25. Blais C, L'Esperance G, Evans GM (1999) Characterization of inclusions found in C-Mn steel welds containing titanium. Sci Tech Weld Join 4(3):143–150

26. Yamata T, Terasaki H, Komizo Y (2009) Relation between inclusion surface and acicular ferrite in low carbon low alloy steel welds. ISIJ Int 49(7):1059–1062

27. Takada A, Terasaki H, Komizo Y (2013) Effect of aluminum content on acicular ferrite formation in low carbon steel weld metals. Sci Tech Weld Join 18(2):91–97

28. Fujiyama N, Shigasato G (2011) Effects of Mn and Al on acicular ferrite formation in SAW weld metal. ISIJ Int 61(5):1614–1622

29. Seo K, Kim Y-M, Evans GM, Kim HJ, Lee C (2015) Formation of Mn-depleted zone in Ti-containing weld metals. Weld World 59:373–380

30. Seo JS, Kim HJ, Lee C (2013) Effect of Ti addition on weld microstructure and inclusion characteristics of bainitic GMA welds. ISIJ Int 53(5):880–886

31. Seo K, Kim Y-M, Kim HJ, Lee C (2015) Characterization of inclusions formed in Ti-containing steel weld metals. ISIJ Int 55(8):1738–1746

32. Seo K, Kim K, Kim HJ, Ryoo H, Evans GM, Lee C (2020) Microstructural and inclusion characteristics of C-Mn steel welds at a minimal level of titanium. Met Mater Int 26(8):1226–1234

33. Kang Y, Jeong S, Kang J-H, Lee C (2016) Factors affecting the inclusion potency for acicular ferrite nucleation in high-strength steel welds. Metal Mater Tran A 47A(6):2842–2854

34. Kang Y, Lee C (2016) Nucleation behavior of acicular ferrite in 1 GPa class high strength steel weld metal. J Weld Join 37(1):21–26 (**in Korean**)

35. North TH, Bell HB, Koukabi A, Craig I (1979) Notch toughness of low oxygen content submerged arc deposits. Weld J 58(12):343s–354s

36. Eijk C, Walmsley J, Grong Ø (2002) Effects of titanium containing oxide inclusions on steel weldability. 6th Int Trends in Weld Res Conf Proc, 15–19 April, Pine Mountain GA, ASM Int: 730–735

37. Lau TW, Sadowski MM, North TH, Weatherly GC (1988) Effect of nitrogen on properties of submerged arc weld metal. Mater Sci Tech 4(1):52–61

38. Grong Ø, Kluken AO, Nylund HK, Dons AL, Hjelen J (1995) Catalyst effects in heterogeneous nucleation of acicular ferrtie. Met Trans A 26A(3):525–534

39. Kojima A, Kasuya T, Tsuruta T, Minami K (2007) Study on application of electrogas arc welding to SM570 steel in bridge fabrication. Trans Jpn Soc Civil Eng A 63(1):1–13 (**in Japanese**)

40. Lee T-K, Kim HJ, Kang BY, Hwang SK (2000) Effect of inclusion size on the nucleation of acicular ferrite in welds. ISIJ Int 40(12):1260–1268

41. Ricks RA, Howell PR, Barritte GS (1982) The nature of acicular ferrite in HSLA steel weld metals. J Mater Sci 17:732–740

42. Seo K, Ryoo H, Kim HJ, Lee C (2019) Quantitative evaluation of nucleation potency of Ti-containing inclusions for acicular ferrite. ISIJ Int 59(6):1105–1112

43. Kayali ES, Corbett JM, Kerr HW (1983) Observations on inclusions and acicular ferrite nucleation in submerged arc HSLA welds. J Mater Sci Lett 2:123–128

44. Grong Ø, Kluken AO, Nylung HK, Dons AL, Hjelen J (1995) Catalyst effects in heterogeneous nucleation of acicular ferrite. Met Trans A 26A(8):525–534

45. Wakoh M, Sawai T, Mizoguchi S (1996) Effect of S content on the MnS precipitation in steel with oxide nuclei. ISIJ Int 36(8):1014–1021

46. Yamamoto K, Hasegawa T, Takamura J (1966) Effect of boron on intra-granular ferrite formation in Ti-oxide bearing steels. ISIJ Int 36(1):80–86